Coastal Sea Level Observations Record the Twentieth-Century Enhancement of Decadal Climate Variability

CHRISTOPHER M. LITTLE[a]

[a] *Atmospheric and Environmental Research, Inc., Lexington, Massachusetts*

ABSTRACT: Changes in the amplitude of decadal climate variability over the twentieth century have been noted, with most evidence derived from tropical Pacific sea surface temperature records. However, the length, spatial coverage, and stability of most instrumental records are insufficient to robustly identify such nonstationarity, or resolve its global spatial structure. Here, it is found that the long-term, stable, observing platform provided by tide gauges reveals a dramatic increase in the amplitude and spatial coherence of decadal (11–14-yr period) coastal sea level (ζ) variability between 1960 and 2000. During this epoch, western North American ζ was approximately out of phase with ζ in Sydney, Australia, and led northeastern U.S. ζ by approximately 1–2 years. The amplitude and timing of changes in decadal ζ variability in these regions are consistent with changes in atmospheric variability. Specifically, central equatorial Pacific wind stress and Labrador Sea heat flux are highly coherent and exhibit contemporaneous, order-of-magnitude increases in decadal power. These statistical relationships have a mechanistic underpinning: Along the western North American coastline, equatorial winds are known to drive rapidly propagating ζ signals along equatorial and coastal waveguides, while a 1–2-yr lag between Labrador Sea heat fluxes and northeastern United States ζ is consistent with a remotely forced, buoyancy-driven, mechanism. Tide gauges thus provide strong independent support for an increase in interbasin coherence on decadal time scales over the second half of the twentieth century, with implications for both the interpretation and prediction of climate and sea level variability.

SIGNIFICANCE STATEMENT: Decadal climate variability influences the frequency and severity of many natural hazards (e.g., drought), with considerable human and ecological impacts. Understanding observed changes and predicting future impacts relies upon an understanding of the physical processes and any changes in their variability and relationship over time. However, identifying such changes requires very long observational records. This paper leverages a large set of tide gauge records to show that decadal time scale coastal sea level variability increased dramatically in the second half of the twentieth century, in widely separated geographic locations. The increase was driven by a shift in the amplitude, spatial pattern, and interbasin coherence of atmospheric pressure, wind, and sea surface temperature variability.

1. Introduction

Earth's climate varies across a wide range of temporal and spatial scales. At multiyear to decadal time scales, such variability is responsible for myriad human and ecological impacts, induced by both persistent anomalies (e.g., extended periods of drought) and the modulation of extreme events (e.g., the risk of tropical cyclone landfalls) (Lee et al. 2021; Seneviratne et al. 2021, 2012). An understanding of decadal variability and its underlying physical mechanisms is thus critical to risk assessment and mitigation efforts. To reduce dimensionality and complexity, climate variability is often described and analyzed using spatiotemporal modes (e.g., Lee et al. 2021). However, both the spatial structure and/or power spectra of these modes can change over time. For example, the centers of action of both El Niño–Southern Oscillation (ENSO) and the North Atlantic Oscillation (NAO) are known to shift position (Kenigson et al. 2018; Kao and Yu 2009; Lee and McPhaden 2010) and exhibit epochs during which different frequency bands are dominant (Higuchi et al. 1999; Sullivan et al. 2016; Kao and Yu 2009). Such changes may be associated with ocean- or atmosphere-mediated interaction between regional modes of variability (e.g., Cai et al. 2019; Martín-Rey et al. 2014; Meehl et al. 2021; Nigam et al. 2020) or with modulation by lower-frequency variability and long-term secular (global) trends (e.g., Lee et al. 2021; Zhang et al. 2019; Liu et al. 2017; Martín-Rey et al. 2018).

There are few stable, continuous instrumental records that can robustly characterize changes in low-frequency (decadal and longer period) climate variability. Evidence for such nonstationarity has largely been derived from tropical Pacific sea surface temperatures (SSTs), often utilizing gridded reanalysis products. Following earlier efforts, Chunhan et al. (2021) assessed decadal variability using a simple index of central Pacific equatorial SSTs, finding a significant well-defined peak at

Corresponding author: Christopher Little, clittle@aer.com

11–12-yr periods between 1951 and 2018 but no evidence for a significant peak between 1871 and 1950. The authors denote this variability, when it is present, as the "quasi-decadal oscillation," a description that dates back to at least Brassington (1997). While other studies often do not explicitly isolate this spectral peak, or address its apparent emergence in the late twentieth century, many have noted enhanced variability in central Pacific SSTs in this frequency band (e.g., Han et al. 2014; Power et al. 2021; Sun and Yu 2009). Other aspects of global climate (e.g., hydroclimate and tropical cyclones) have also been shown to exhibit closely associated variability and coincident increases in decadal power (e.g., Liu et al. 2019; Lyu et al. 2017; Wang et al. 2010, 2014).

The regional scope of most studies obscures interpretations of the drivers and spatial coherence of amplified decadal variability. Furthermore, instrumental records are often sparse before the mid-twentieth century, leaving open the possibility that data limitations play a role in the relatively weak variability observed in earlier periods. Capturing modulations in low-frequency variability at a global scale requires a long (approximately centennial) stable record with sufficient spatial coverage. Tide gauges have recorded relative sea level at coastal locations since the eighteenth century, with increasingly dense coverage in time and space (Holgate et al. 2013), and thus constitute a valuable means to identify changes in decadal variability. Indeed, tide gauges have been used to identify and interpret interannual to multidecadal ocean and climate variability, including regional and global modes (Han et al. 2019, and references within). At lower frequencies, several studies using these records have found evidence for nonstationarity and/or temporal changes in the spatial structure of coastal sea level variability (e.g., Han et al. 2019; Kenigson et al. 2018; Woodworth et al. 2017).

For example, Little et al. (2021) showed that the time-dependent amplitude of 10–15-yr period variability is a dominant control on the spatial structure of annual mean sea level variability along the U.S. East Coast. No robust relationship with North Atlantic climate modes was apparent. However, the timing of order-of-magnitude changes in power along the northeast U.S. coast, and the frequency band in which power is enhanced, closely match those highlighted in studies of the central Pacific SST record.

Most previous studies of interannual-to-decadal sea level variability have examined spatial structure and underlying mechanisms at an a priori defined regional scale. Furthermore, many studies focus primarily on the second half of the twentieth century. Here, I extend previous analyses of the coastal sea level record by identifying linkages across geographically widespread and dynamically disconnected regions of the global ocean over the 1900–2019 period. Rather than isolating a "common" or "global" component of sea level variability (e.g., Dangendorf et al. 2017; Kopp et al. 2016), I identify coherent regional variations that are associated with common underlying global climate forcing but may vary in amplitude and/or phase. This analysis helps consolidate disparate evidence for enhanced late twentieth-century climate variability across several regions and relevant climate variables,

while revealing the nonstationary global drivers of regional sea level variability.

2. Data and methods

a. Tide gauges

I analyze 64 monthly mean tide gauge records (Tables S1 and S2 in the online supplemental material), retrieved from the Permanent Service for Mean Sea Level Revised Local Reference (PSMSL RLR) database on 1 July 2020 (Holgate et al. 2013). Tide gauge records are included if they are >95% complete during the 1930–2015 period. The Tuapse tide gauge record was not included in this analysis due to an apparent discontinuity. Monthly records for all tide gauges from 1900 to 2019 are shown in Figs. S1–S4.

I have chosen a cutoff year of 1930 to sufficiently resolve periods of enhanced and muted decadal variability. However, due to the sparsity of long tide gauge records outside North America and Europe, this choice leaves only two records from outside these regions: Balboa, in central America, and Sydney, in Australia. The implications of geographic sparsity are discussed in section 4a.

Tide gauges record long-term increases in relative sea level, with contributions from various local, regional, and global processes, including vertical land motion (e.g., Stammer et al. 2013). As this analysis focuses on sea level fluctuations related to climate variability, I linearly detrend monthly records over the period of record. After removing the trend, gaps in monthly records are filled by zeros (Figs. S1–S4) before calculating annual means (Figs. S5–S8). Results are insensitive to the details of the gap-filling algorithm or the assumption of a linear long-term trend. All subsequent analyses are performed on detrended annual mean values (subsequently denoted as ζ) over the 1900–2019 period.

b. Reanalysis

To compare tide gauge records to other related climate variables, I employ NOAA's Twentieth Century Reanalysis, version 3 (20CR3; Slivinski et al. 2019), downloaded on 1 February 2022. The ζ variability is compared with several surface variables from 20CR3, including skin temperature ("skt"; sea surface temperature over the ocean and surface air temperature over land), zonal and meridional momentum flux ("uflx" and "vflx", respectively), and sensible and latent heat flux ("shtfl" and "lhtfl", respectively). Analysis is performed only on the sum of sensible and latent heat fluxes, denoted by Q (positive for heat fluxes out of the ocean).

I utilize 20CR3 output over the 1900–2015 period, calculating annual averages from monthly mean, ensemble mean, output. At each grid point, time series are linearly detrended over the 1900–2015 period. In some figures (Figs. 4, 5, 10, and 11), each variable is smoothed using a 3° Gaussian filter, then interpolated to a 2° horizontal grid. Here, I refer to skin temperature as surface temperature (T_S). Gridded sea surface temperature products, not shown, provide similar results to those shown for T_S over the ocean.

c. Statistical analyses

To investigate evidence for time-varying decadal variability in ζ and related climate variables, I calculate continuous wavelet power spectra and wavelet coherence from annual time series. Complete wavelet power spectra for ζ at all tide gauges are shown in Figs. S9–S14. Wavelet analysis was performed using publicly available MATLAB code (Grinsted et al. 2004) and parameters described in Little et al. (2021). Results are insensitive to reasonable alternative parameter choices.

Uncertainty is assessed using Monte Carlo techniques. For each tide gauge, I generate 1000 synthetic red noise time series of the same length and with identical lag-1 autocorrelation coefficients. Power and coherence are considered significant if they are greater than the 95th percentile value of the synthetic time series.

3. Results

a. Coherent decadal ζ variability

In Little et al. (2021), the detrended annual mean relative sea level (ζ) along the northeastern United States coastline between Cape Hatteras and Boston was shown to exhibit a significant increase in decadal power beginning in the second half of the twentieth century. Within this region, the Battery tide gauge in New York City is the only record spanning the entire twentieth and twenty-first centuries. This time series, denoted as ζ_{NYC} and highlighted in Fig. 1a, shows a clear shift toward more pronounced low-frequency variability over the mid-to-late twentieth century. Wavelet analysis (Fig. 1b) indicates an order-of-magnitude increase in power at a 12.4-yr period beginning in approximately 1960 that is statistically significant after 1980.

At a 12.4-yr period, increases in power of a similar amplitude are also evident at many other tide gauges over the second half of the twentieth century (Fig. 1c; see also Figs. S9–S14). Focusing on the time period centered on 1980 (Fig. 1d), high power is evident in all U.S. east coast tide gauges between Boston and Cape Hatteras. High (although not significant) variability is evident to the south, along the east and Gulf of Mexico coasts, beginning as early as ~1940. Large increases in power relative to the first half of the twentieth century are apparent along the western North American coast, especially between San Francisco and Vancouver Island, with smaller increases along the southern California coastline. Despite many long and continuous tide gauge records, European locations exhibit a notable lack of ζ power at this frequency band throughout the twentieth century.

The sparsity of long records in other regions makes it difficult to assess large-scale evidence for enhanced power elsewhere. However, two geographically isolated tide gauges also exhibit significant increases in decadal power over this time period (Balboa, on the Pacific coast of Panama, and Sydney, Australia).

At tide gauges that show an enhancement of power in the second half of the twentieth century, ζ is coherent with ζ_{NYC} (Fig. 2). For example, ζ at the Seattle tide gauge, highlighted in Figs. 2a and 2b, is significantly coherent with ζ_{NYC} between 1960 and 1990. Although not discussed further, there is also evidence of coherence after 1980 at 2–4-yr periods, perhaps associated with the 1982 El Niño event.

While the coherence, phase, and amplitude of ζ variability at a 12.4-yr period vary at the scale of individual tide gauges (Figs. 2c,d; see also Figs. S15–S20), some general large-scale patterns are evident. High coherence is evident from Boston to Sewell's Point, north of Cape Hatteras [see Little et al. (2021) for more details on the temporal evolution of coherence along the U.S. east coast]. However, ζ is also coherent with ζ_{NYC} along the majority of the western North American coastline, with the highest values along the U.S. coast north of San Francisco. In this region, over the epoch centered on 1980, ζ leads ζ_{NYC} by between 1.3 and 2.0 years, with a mean value of 1.7 years. South of San Francisco, coherence is lower, and leads are slightly longer (between 2.2 years at San Diego and 2.8 years at La Jolla; 2.5 years at Balboa). In contrast, ζ at Sydney, Australia lags ζ_{NYC} by approximately 4 years (i.e., out of phase with ζ on the western North American coast). In this frequency band, coherence with ζ at all European tide gauges is low over the entire period of record.

b. Drivers of coherent ζ variability

Figures 1 and 2 indicate the contemporaneous emergence of heightened decadal power at many global tide gauges. Several lines of evidence argue against an origin in global mean sea level variability, including the large amplitude of this signal (~5–10 cm), temporal lags between geographic regions, and a lack of evidence for coherent variability in Europe. With the additional assumption that oceanic propagation of a sea level signal between the northwest Atlantic and Pacific Oceans is unlikely, these results imply a role for global-scale shifts in atmospheric variability, perhaps linked via teleconnections. The remainder of this paper seeks to address the atmospheric forcings and oceanic propagation pathways responsible for 1) amplification of decadal power in ζ and 2) the linkage and temporal lags between ζ across different regions. The variability of ζ may be driven by many climate processes (Woodworth et al. 2019). However, previous analyses suggest that surface heat and/or momentum fluxes (both local and nonlocal) are the dominant drivers of coastal ζ variability in the regions and frequency bands highlighted in the previous section (e.g., Han et al. 2019; Hong et al. 2000; Thompson et al. 2014). To inform the nature of surface forcing responsible for ζ variability, I again utilize coherence analyses, applied to gridded surface momentum and heat fluxes over the 1900–2015 period from NOAA's 20CR3 (Slivinski et al. 2019). Instead of a single tide gauge, I examine the coherence of surface fields with a composite ζ record (ζ_{NE}; Fig. 3): The arithmetic mean of ζ across the six northeastern United States tide gauges that are coherent and in phase in Fig. 2. As for ζ_{NYC}, decadal power in ζ_{NE} increases by approximately 14 times between 1945 and 1980, but with a slightly earlier onset (Fig. 3b).

While compositing is not essential, it reduces noise from inter-tide gauge variations (Fig. 3a), and simplifies the presentation of
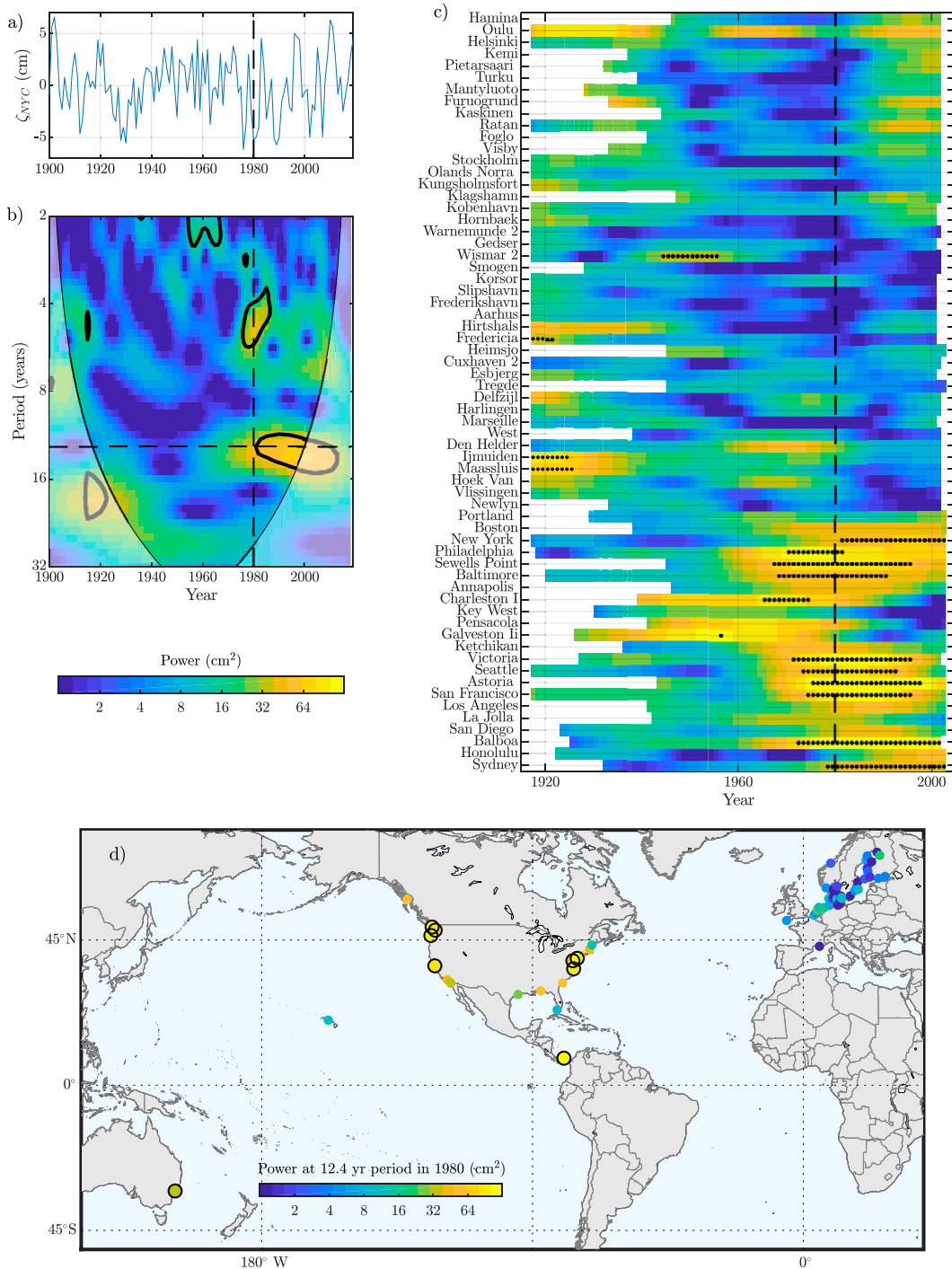
FIG. 1. (a) Annual mean time series and (b) continuous wavelet power spectra of detrended sea level at the New York City tide gauge (ζ_{NYC}) over the 1900–2019 period. In (b), significance at the $p < 0.05$ level [relative to 1000 resampled time series with identical AR(1) coefficients] is shown with black contours; the horizontal dashed line corresponds to a period of 12.4 years, the vertical dashed line corresponds to 1980, and the transparent mask indicates the cone of influence. (c) Power centered on a period of 12.4 years (cm^2) for all tide gauges, only shown for times outside the cone of influence; significance at the $p < 0.05$ level is shown with stippling. (d) Wavelet power for ζ at each tide gauge, centered on 1980 at a period of 12.4 years. Significance at the $p < 0.05$ level is indicated with black outlines.
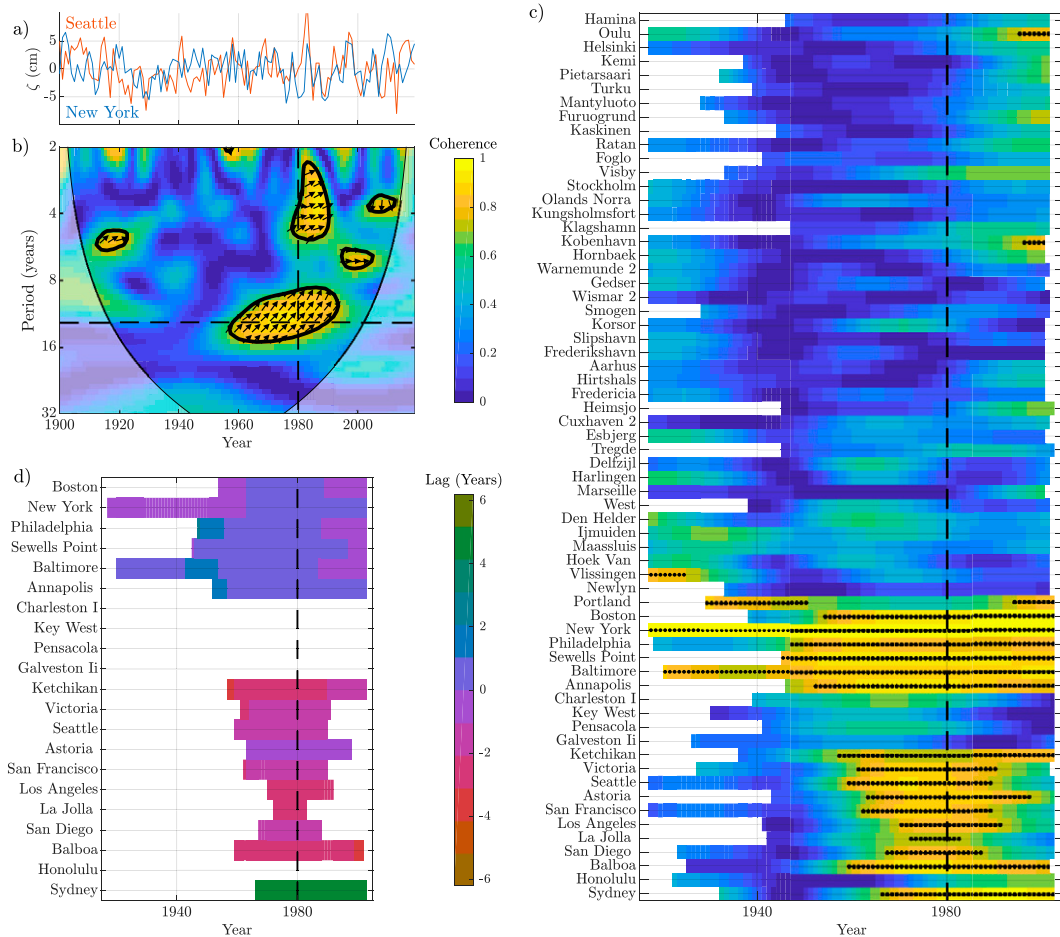
FIG. 2. (a) The ζ at the Seattle (orange line; cm) and New York City (blue) tide gauges over the 1900–2019 period, and (b) their magnitude-squared wavelet coherence. Arrows in (b) indicate the phase relationship (arrows point up if Seattle leads by 90°; they point right if time series are in phase). A transparent mask indicates the cone of influence. Black lines denote significance at the $p < 0.05$ level relative to 1000 resampled time series with the same AR(1) regression coefficients. (c) Wavelet coherence between ζ_{NYC} and ζ at each tide gauge, centered on a period of 12.4 years, over the time period of coincident measurements. (d) The phase lag between ζ_{NYC} and ζ at each tide gauge, at a period of 12.4 years, at 22 tide gauges [yr, where positive values indicate ζ_{NYC} leads; only shown where values in (c) are significant at $p < 0.05$].

results. Later results are insensitive to the individual tide gauges used in the composite, and to identical analyses performed using tide gauges from other regions (as long as they are significantly coherent with ζ_{NE}). The validity of this approach is confirmed later (see Figs. 8 and 9), in which regional forcings highly coherent with ζ_{NE} are also coherent with ζ in other locations.

Figures 4 and 5 summarize the twentieth-century changes in coherence of ζ_{NE} with wind stress (τ_x and τ_y) and surface heat flux (Q), as well as changes in the local power in each surface forcing field. Time periods centered on 1945 and 1980 are highlighted; other epochs are shown in Figs. S21–S26.

There is a dramatic increase in coherence at a 12.4-yr period across many regions of the global ocean over the second half of the twentieth century. In the period centered on 1945 (Fig. 5), despite evidence for relatively high decadal power in each surface forcing field (e.g., zonal wind stress in the North Atlantic subpolar gyre), ζ_{NE} is only coherent with

surface forcing over a few widely separated regions of the global ocean. By 1980 (Fig. 4), coherence between τ and ζ_{NE} extends more broadly through the western Atlantic subpolar gyre into Davis Strait, southwestward toward the North American coastline and the North Atlantic Current. Power in τ increases substantially over the same region, particularly for τ_y in the Labrador Sea. Perhaps more surprisingly, coherence between τ and ζ_{NE} is highest in distant regions, including the tropical Atlantic, central equatorial Pacific and the Pacific sector of the Southern Ocean (all of which also exhibit approximately an order of magnitude increase in the decadal variability of τ).

Coherence between ζ_{NE} and Q (Fig. 4c) also increases over many regions of the global ocean, often in conjunction with τ, although its spatial structure is more localized. Coherence in the Labrador Sea is particularly strong in the late twentieth century, approaching a value of 1. This increase in coherence
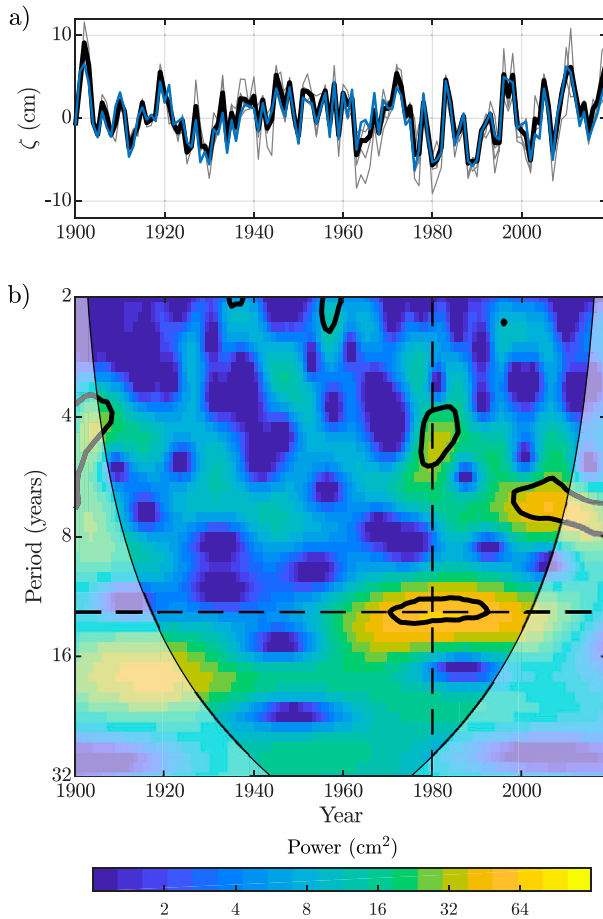
a)

b)

FIG. 3. (a) The ζ_{NE} (thick black line) and ζ from individual tide gauges (Annapolis, Baltimore, Sewell's Point, Philadelphia, New York City, and Boston), with ζ_{NYC} in blue (ζ from other tide gauges is shown with gray lines). (b) As in Fig. 1b, but for ζ_{NE}.

occurs along with a simultaneous increase in Q variability extending southward from the Labrador Sea along the northwest Atlantic coastline toward Cape Hatteras. The dramatic increase in spatial coherence within and across surface forcing fields indicates that coherence between widely separated tide gauges (Fig. 2) originates from an increase in the strength of interbasin atmospheric teleconnections. However, Fig. 4 reveals multiple forcings that could plausibly induce a twentieth century increase in ζ variability. To identify the most relevant regions of surface forcing and to infer underlying mechanisms driving ζ variability, I examine the northwestern Atlantic and northeastern Pacific in more quantitative detail in the following sections. Coastlines in these two regions both exhibit a large increase in ζ power over the twentieth century, and have observational records that are relatively spatially and temporally well resolved.

1) NORTHEASTERN U.S. COASTLINE

At interannual time scales, northeastern U.S. ζ is known to be influenced by both remote (Little et al. 2019; Minobe et al. 2017; Roussenov et al. 2008) and local (Andres et al. 2013;

Li et al. 2014; Piecuch et al. 2018a, 2016) momentum and buoyancy forcing. Although there is evidence that local forcing dominates interannual and higher frequencies, while remote forcing becomes important at lower frequencies, the importance of each driver at approximately decadal time scales is unclear (Little et al. 2019, 2017; Thompson 1986; Wang et al. 2022).

Figure 6a isolates the importance of remote heat fluxes in the period of high decadal variability by showing coherence (shading) only in regions where it is significant and where power increases by greater than an order of magnitude between 1945 and 1980. The relevance of the Labrador Sea, suggested by Fig. 4c, is clear, and is further strengthened by examining the twentieth-century evolution of the Labrador Sea areal-mean heat flux (Q_{LS}; Figs. 6b–d). Power in Q_{LS} shows close correspondence to that in ζ_{NE}, increasing rapidly between 1950 and 1980 and decreasing thereafter. Coherence analysis (Fig. 6d) indicates that, over the period of enhanced power, ζ_{NE} is highly coherent with Q, leading by approximately 4.5 years. Alternatively, ζ_{NE} can be interpreted to lag the negative of Q by approximately 1.5–2 years.

The latter interpretation is consistent with a pathway in which negative (in 20CR3, into the ocean) Labrador Sea heat fluxes drive upper ocean warming (i.e., negative density/positive steric sea level) anomalies that are advected southward along the slope and/or deep western boundary current, in turn driving positive ζ_{NE} anomalies. An approximately 1.5-yr lag is consistent with the advective time scale of the slope current (New et al. 2021; Wang et al. 2022) but is smaller than expected in deeper layers (Le Bras et al. 2017), while a role for density anomalies is consistent with correlations between steric height in the southwestern subpolar gyre and ζ along the northeastern United States coastline found in Frederikse et al. (2017). However, interactions between density anomalies and changes in the transport of various currents, and the means by which these offshore changes are communicated to and along the coast, are complex and deserve more detailed analysis (see section 4d).

As noted earlier, changes in τ evident in Figs. 4 and 5 may also influence ζ. The ability of these mechanisms to account for enhanced decadal variability in ζ_{NE} is examined, as for heat fluxes, in Fig. 7. For simplicity, I show only zonal wind stress and wind stress curl ($\nabla \times \tau$), both of which are known drivers of ζ variability on the United States coastline.

Two regions of increases in power and coherence are evident. The first, in zonal wind stress (Fig. 7a), extends from the Grand Banks toward the central Atlantic. The second, in wind stress curl (Fig. 7b), lies in the interior of the subtropical gyre. Each area-averaged quantity exhibits a similar temporal evolution in power (Figs. 7e,f), and τ_x and $\nabla \times \tau$ are roughly out of phase with each other when they are significantly coherent with ζ_{NE} (Figs. 7g,h). These relationships are closely linked because these fields are not independent: heightened τ_x variability drives a meridionally displaced out-of-phase increase in $\nabla \times \tau$ power.

Furthermore, neither appears likely to be a primary driver of decadal variability. First, there is no clear mechanism linking either forcing region, both of which are in quadrature with ζ_{NE},
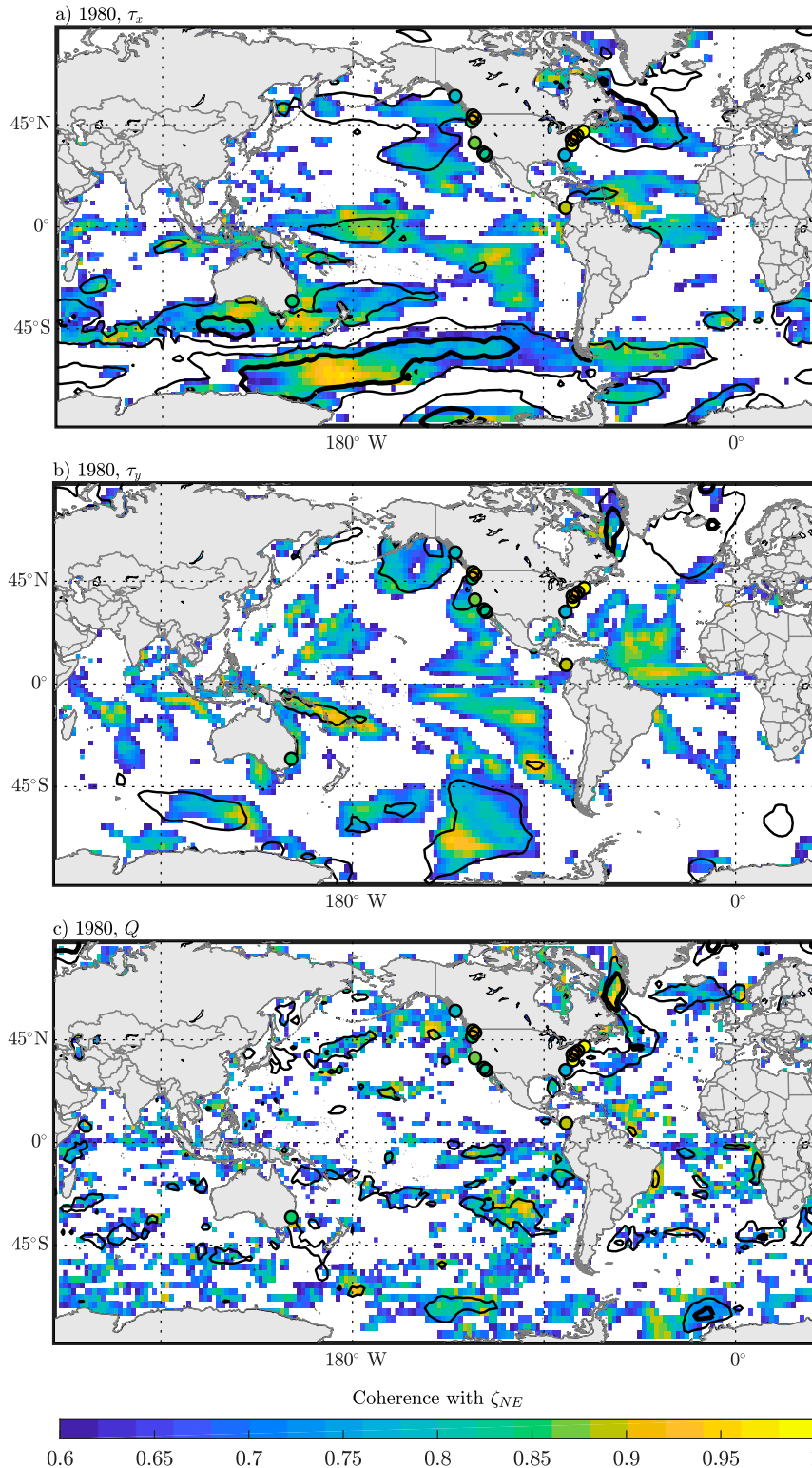
Fig. 4. (a) Wavelet coherence (shading) between ζ_{NE} and zonal wind stress (τ_x) from 20CR3, on a 2° horizontal grid, centered on a period of 12.4 years and the year 1980. Contours indicate wavelet power centered on a period of 12.4 years; the thick (thin) line is 1.5×10^{-3} (0.3×10^{-3}) N^2 m^{-4}. Circles show magnitude-squared wavelet coherence between ζ_{NE} and ζ at each tidegauge where it is significant at $p < 0.05$. (b) As in (a), for wavelet coherence between ζ_{NE} and meridional wind stress (τ_y). (c) As in (a), for wavelet coherence between ζ_{NE} and the sum of latent and sensible heat fluxes (Q); the thick (thin) line is 1000 (200) W^2 m^{-4}. Although the $p < 0.05$ significance level between ζ_{NE} and each surface field varies depending on the location and variable, it is generally around 0.7.
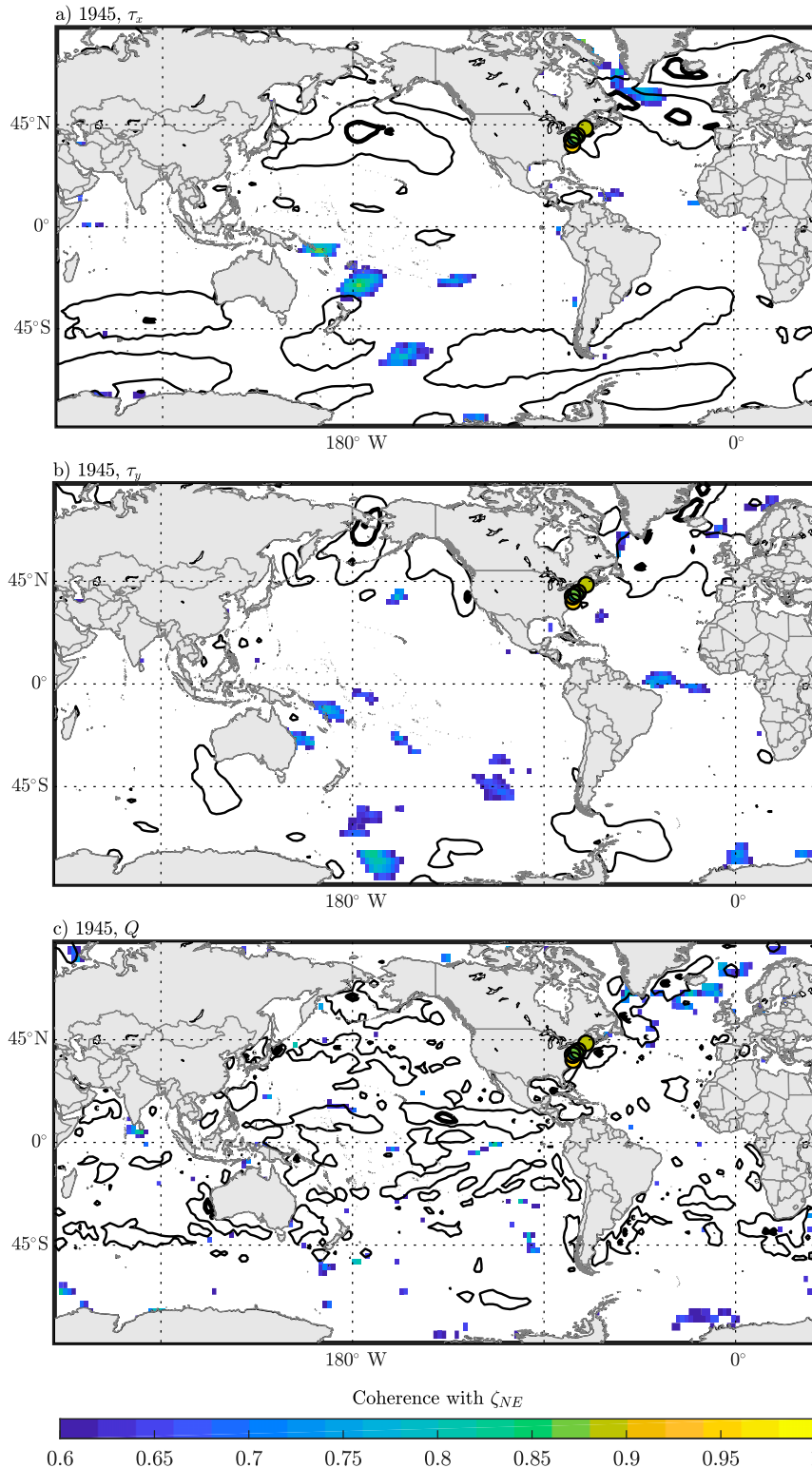
Fig. 5. (a) Wavelet coherence (shading) between ζ_{NE} and zonal wind stress (τ_x) from 20CR3, on a 2° horizontal grid, centered on a period of 12.4 years and the year 1945. Contours indicate wavelet power centered on a period of 12.4 years; the thick (thin) line is 1.5×10^{-3} (0.3×10^{-3}) N^2 m^{-4}. Circles show magnitude-squared wavelet coherence between ζ_{NE} and ζ at each tide gauge where it is significant at $p < 0.05$. (b) As in (a), but for wavelet coherence between ζ_{NE} and meridional wind stress (τ_y). (c) As in (a), for wavelet coherence between ζ_{NE} and the sum of latent and sensible heat fluxes (Q); the thick (thin) line is 1000 (200) W^2 m^{-4}. Although the $p < 0.05$ significance level between ζ_{NE} and each surface field varies depending on the location and variable, it is generally around 0.7.
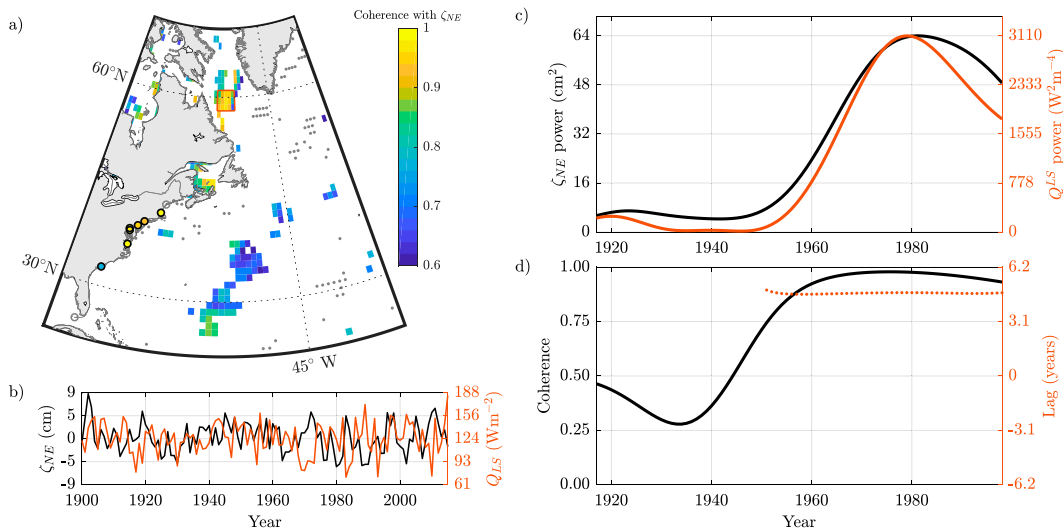
FIG. 6. (a) Wavelet coherence (shading) between ζ_{NE} and the sum of latent and sensible heat fluxes (Q) from 20CR3, on a 2° horizontal grid, centered on a period of 12.4 years and the year 1980. Coherence is only shown (with shading) where wavelet power in Q in 1980 is at least 10 times larger than in 1945. Stippling indicates that wavelet power in 1945 is 10 times larger than in 1980. Circles show magnitude-squared wavelet coherence between ζ_{NE} and ζ at a period of 12.4 years in 1980 (only shown where significant). (b) Annual mean time series of ζ_{NE} (black) and Q_{LS} [area-averaged Q over the Labrador Sea, in the region 58°–61°N, 55°–60°W; orange box in (a)]. (c) Wavelet power in Q_{LS} (orange) and ζ_{NE} (black), centered on the 12.4-yr period. (d) Coherence between Q_{LS} and ζ_{NE} and phase (orange, in years, where positive values indicate ζ_{NE} leads) centered on the 12.4-yr period. Phase is only shown where coherence is significant at $p < 0.05$.

to sea level north of Cape Hatteras. Second, coherence in both regions is only marginally significant and is substantially smaller than Q_{LS}. Third, the temporal evolution of power exhibits an earlier peak than that of ζ_{NE}. I thus propose that the coherence between τ with both ζ_{NE} is driven by basin-scale changes in the large-scale wind field associated with Q_{LS}, rather than through a causal mechanism.

Consistent with Fig. 4, Fig. 7 does not show increases in coherence between ζ_{NE} and local alongshore wind stress (or large increases in local wind stress power), which has been highlighted in observational studies as a primary driver of ζ_{NE} (Andres et al. 2013; Li et al. 2014; Piecuch et al. 2016). Time series of alongshore winds (not shown) are inconsistent with the temporal evolution of power and coherence in ζ_{NE} at decadal periods, suggesting this mechanism is of limited importance over longer time scales. There is also no evidence for coherence with large-scale changes in $\nabla \times \tau$ in the subpolar gyre, as noted in recent studies of decadal variability (Chafik et al. 2019), potentially indicating that these basin-scale relationships do not persist at the coast.

2) WESTERN NORTH AMERICAN COASTLINE

On the western North American coastline, wind stress curl and offshore buoyancy fluxes do not play a large role in ζ variability, as Rossby waves propagate westward. Thus ζ is forced largely by local alongshore winds and equatorial winds, which induce sea level variability that propagates along the equatorial and coastal waveguides. At interannual time scales, alongshore

and equatorial zonal wind stress forcing has been shown to explain almost all ζ variability along the U.S. West Coast (Chelton and Davis 1982; Enfield and Allen 1980; Thompson et al. 2014).

Figure 4 indicates that, at a 12.4-yr period, ζ_{NE} is coherent with equatorial zonal wind stress, particularly in the central Pacific, and (slightly less) coherent with meridional wind stress along the coast. The relative roles of these forcings, and any variation in their importance along the coast, require comparison with individual tide gauge records. Thus, as in Fig. 7, I compare regional mean wind stresses in each region to ζ in two locations along the coastline (Figs. 8 and 9).

At the Balboa tide gauge (ζ_{BAL}), only equatorial wind stress is relevant. Figure 8a isolates two equatorial regions of coherence that exhibit a greater than 10 times increase in decadal τ_x power: the central Pacific (CP; defined as 5°S–5°N, 180°E–165°W) and the eastern Pacific (EP; defined as 3°S–3°N, 90°–115°W). Between these two regions, there is a decrease in wind stress power, indicating a pronounced zonal shift in wind centers of action through the twentieth century.

Wavelet power in ζ_{BAL} in the decadal frequency band increases at roughly the same rate as τ_{CP} beginning in approximately 1960, suggesting a strong and persistent relationship (Fig. 8d). The associated lag of approximately one year (Fig. 8f) is longer than expected for eastward propagating, equatorially trapped Kelvin waves, but is consistent with the annual time resolution of this analysis. In contrast, the increase in power in the eastern Pacific (τ_{EP}; Fig. 8e) is smaller, and
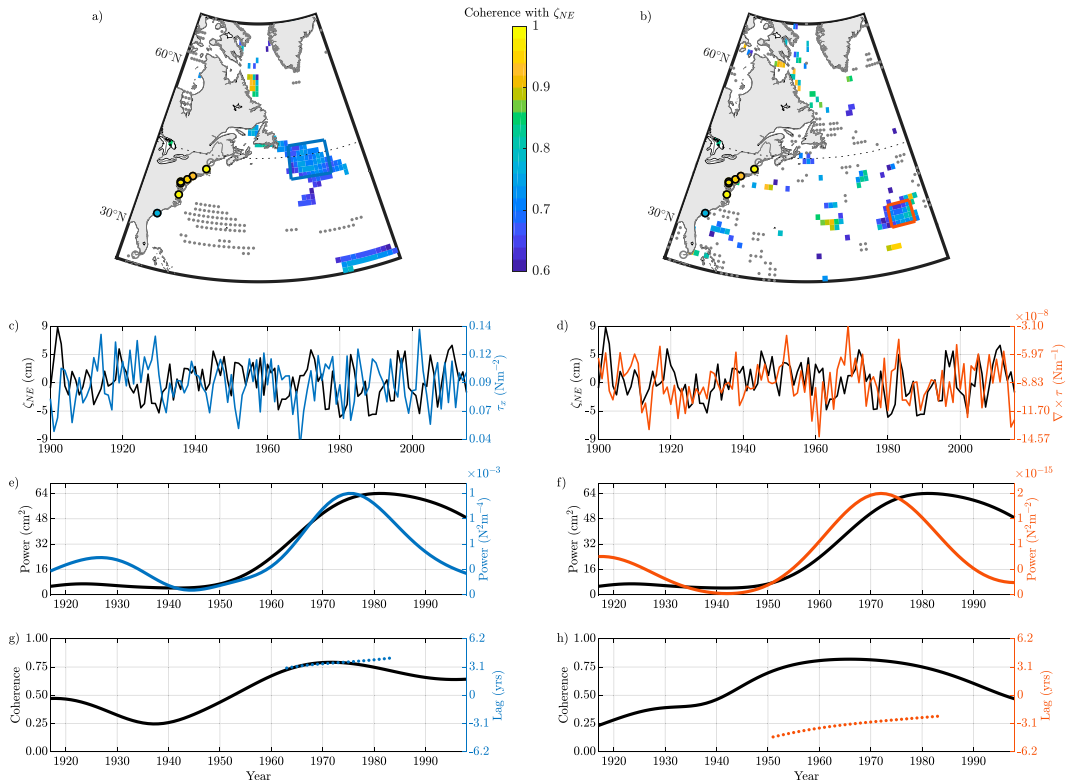
FIG. 7. (a) Wavelet (shading) coherence between ζ_{NE} and τ_x from 20CR3 over the northwest Atlantic Ocean, on a 2° horizontal grid, centered on a period of 12.4 years and the year 1980. Coherence is only shown where wavelet power in τ_x in 1980 is at least 10 times larger than in 1945. (b) As in (a), but for $\nabla \times \tau$. (c) Annual mean time series of ζ_{NE} (black) and τ_x, area-averaged over the region 41°–47°N, 40°–50°W region [blue box in (a)]. (e) Wavelet power in τ_x (blue) and ζ_{NE} (black), centered on the 12.4-yr period. (g) Coherence between τ_x and ζ_{NE} and phase (blue dotted line, in years, where positive values indicate ζ_{NE} leads) centered on the 12.4-yr period. Phase is only shown where coherence is significant at $p < 0.05$. (d),(f),(h) As in (c),(e),(g), but for ζ_{NE} and $\nabla \times \tau$, area-averaged over the 31°–35°N, 35°–40°W region [orange box in (b)].

occurs later in time. The terms τ_{EP} and ζ_{BAL} are also less co-herent, and roughly in quadrature (Fig. 8g), for which there is no clear explanation.

Central tropical Pacific winds alone cannot explain the along-coast variation in the amplitude of ζ variability, which reaches a maximum in the Pacific Northwest (Fig. 1). A purely equatorially driven signal would likely exhibit a de-crease in power with (northward) distance along the coast. I thus consider the potential for augmentation by alongshore wind stress (τ_{AS}), which is known to have a pronounced influ-ence on ζ north of San Francisco (Chelton and Davis 1982; Enfield and Allen 1980; Thompson et al. 2014), using the Seattle tide gauge (ζ_{SEA}) as an example.

In Fig. 9, τ_{AS} is calculated over a relatively large region of the coastline to account for forcing from the south, and meridi-onal winds are used as a proxy of alongshore winds given their higher coherence with ζ and the approximately meridional ori-entation of the coastline. Results are insensitive to this choice due to the large-scale spatial coherence of the wind field.

In Seattle, a strong relationship with τ_{CP} (Fig. 9e; coherence > 0.75) is retained between approximately 1950 and approximately 1990, with a slightly longer phase lag than that seen at Balboa,

suggesting equatorial forcing remains relevant. However, the phase relationship between τ_{CP} and ζ_{SEA} is less stable over time, and coherence declines after ~1970. Coincident with this decline, coherence between τ_{AS} and ζ_{SEA} increases in magnitude, approaching 1 after 1990, reflecting the impor-tance of alongshore winds in this location (Fig. 9d). The period of highest power in ζ_{SEA} coincides with the peak in τ_{AS}, suggesting that enhancement of decadal ζ variability in the Pacific Northwest (the largest increase observed at any tide gauges globally; Fig. 1) is driven by the super-position of coherent, reinforcing, drivers (Thompson et al. 2014). At locations between Balboa and San Francisco (not shown), ζ power, and its coherence with τ_{AS}, is smaller, sug-gesting that the changes in alongshore winds are less effec-tive in modulating ζ (likely due to the orientation of the coastline).

The increase in power in τ_{AS} centered on 1945 (Fig. 9c), of comparable amplitude to the late twentieth-century increase, is not evident in ζ_{SEA} (although a small maximum in coher-ence is evident). It is unclear whether this is due to limitations of the reanalysis, or an offsetting driver of ζ variability over this epoch (see section 4a).
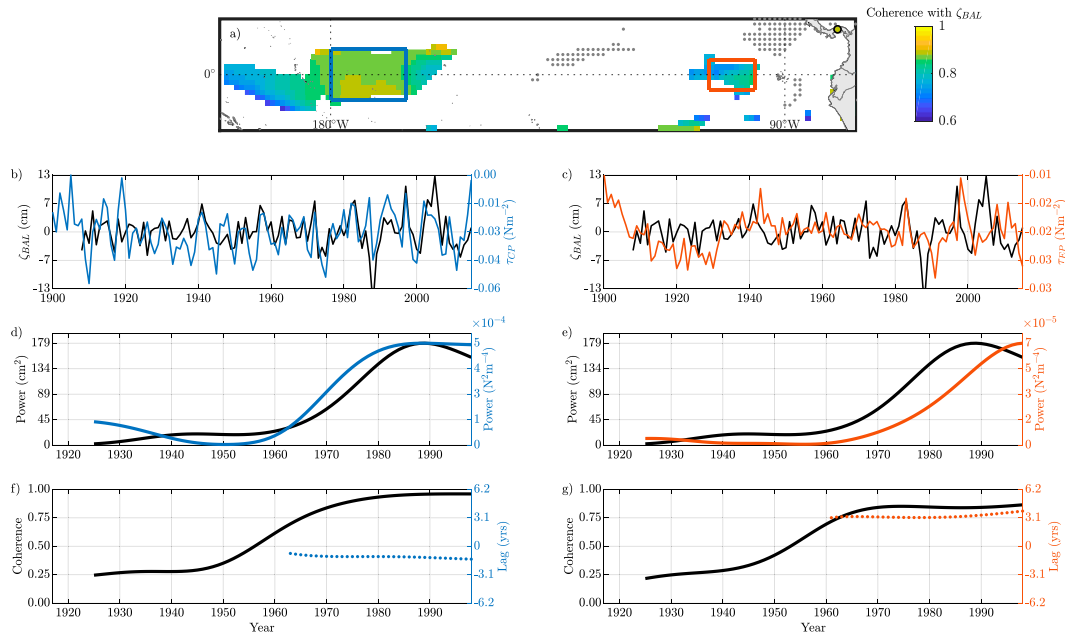
FIG. 8. (a) Wavelet coherence (shading) between ζ_{BAL} and τ_x from 20CR3 over the tropical Pacific Ocean, on a 2° horizontal grid, centered on a period of 12.4 years and the year 1980. Coherence is only shown where wavelet power in τ_x in 1980 is at least 10 times larger than in 1945. (b) Annual mean time series of ζ_{BAL} (black) and τ_x, area-averaged over the central Pacific region [τ_{CP}; blue box in (a)]. (d) Wavelet power in τ_{CP} (blue) and ζ_{BAL} (black), centered on the 12.4-yr period. (f) Wavelet coherence between τ_{CP} and ζ_{NE} and phase (blue dotted line, in years, where positive values indicate ζ_{BAL} leads) centered on the 12.4-yr period. Phase is only shown where coherence is significant at $p < 0.05$. (c),(e),(g) As in (b),(d),(f), but for ζ_{BAL} and τ_x, area-averaged over the eastern Pacific region [τ_{EP}; orange box in (a)]. The ζ_{BAL} is detrended relative sea level at the Balboa, Panama, tide gauge.

c. Relationship to global climate

Earlier sections indicate that increases in decadal ζ variability are related to increases in the amplitude of surface momentum and heat fluxes in key geographic regions. These fluxes are, in turn, related to other aspects of global climate, including well-observed surface atmospheric fields, such as temperature (T_S) and air pressure (P_S). I examine the coherence of these fields with ζ_{NE} in Fig. 10.

Beyond their influence on Q_{LS}, P_S and T_S are not likely to be causally related to ζ_{NE}. However, the regions of coherence, as well as the associated phase relationships, provide a more complete picture of large-scale climate variability that can help elucidate mechanisms driving the apparent periodicity of this global mode and/or physical linkages between different regions and variables (see section 4c).

Consistent with Figs. 4 and 5, coherence between the surface atmospheric state and ζ_{NE} (Fig. 10) extends over a large portion of the global ocean in the second half of the twentieth century, with almost no regions of significance in 1945. In the epoch centered on 1980, the largest and most spatially coherent T_S anomalies associated with decadal ζ_{NE} variability are in the south tropical Atlantic and central tropical Pacific oceans. In the Pacific, the spatial structure of coherent T_S variability is consistent with the well-known tripole pattern (Han et al. 2014; Henley et al. 2015; Lyu et al. 2017) but also extends to the South Pacific Ocean. As for Q_{CP}, there is a large

increase in T_S power in the central tropical Pacific. There is also high coherence with T_S in the North Atlantic near the path of the detached Gulf Stream. Coherence between ζ_{NE} and P_S is highest in the western Indian Ocean, but is significant over much of Earth's surface, including the eastern subtropical Pacific, the South Atlantic (where ζ_{NE} is also coherent with SSTs), the North American high latitudes from Siberia to Greenland, and the Pacific sector of the Southern Ocean.

At the large scale, the centers of action evident in Fig. 10 exhibit well-defined phase relationships (Fig. 11). The Pacific tripole pattern is evident, and T_S in the tropical Pacific and Atlantic are approximately out of phase. SSTs near the Gulf Stream detachment lag ζ_{NE} by approximately 4–5 years.

Figure 11b shows a meridional P_S tripole extending southeastward toward Antarctica from the tropical Indian Ocean, suggestive of a stationary Rossby wave response to tropical variability (e.g., Branstator 2002; Li et al. 2021). The P_S in the Indian and south tropical Atlantic Oceans are in phase, leading ζ_{NE} by 1–2 years, while P_S over the Pacific is approximately out of phase with the other ocean basins. In the high northern latitudes, there is a band of (approximately) in-phase coherence from Siberia to the tip of Greenland.

These phase relationships are consistent with those found in Figs. 6–9. For example, Fig. 6a indicates that coherence with Q_{LS} is quite localized and has a well-defined phase relationship (Q_{LS} minima lead ζ_{NE} by 1–2 years). The P_S maxima
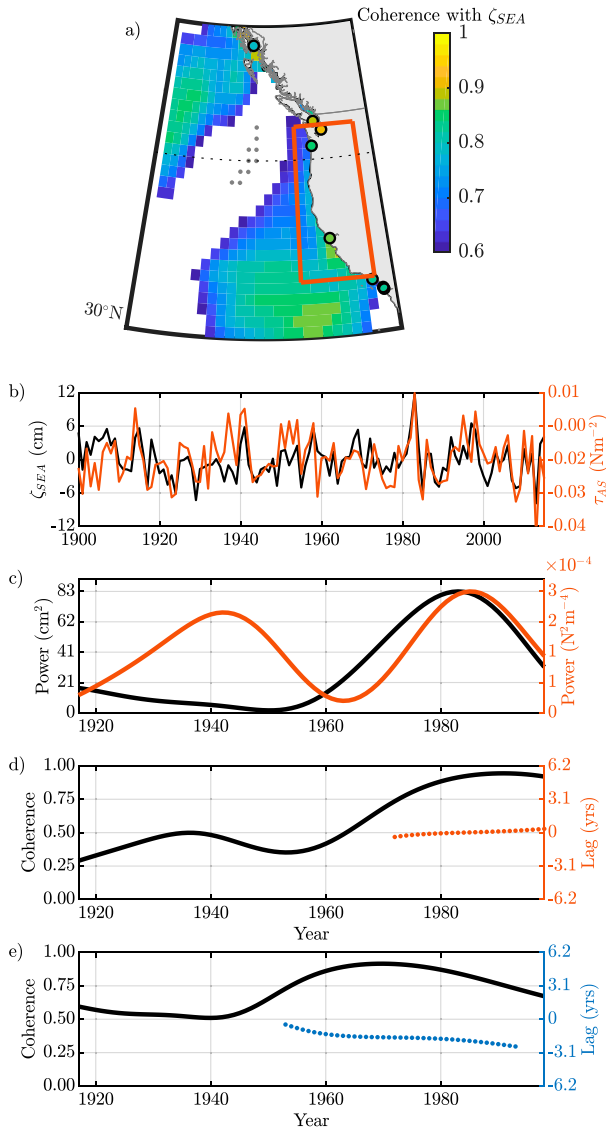
FIG. 9. (a) Wavelet coherence (shading) between ζ_{SEA} and τ_{AS} from 20CR3 near the western North American coastline, on a 2° horizontal grid, centered on a period of 12.4 years and the year 1980. Coherence is only shown where wavelet power in τ_{AS} in 1980 is at least 10 times larger than in 1945. (b) Annual mean time series of ζ_{SEA} (black) and τ_{AS}, area-averaged over the region 34°–45°N, 118°–126°W [orange box in (a)]. (c) Wavelet power in τ_{AS} (blue) and ζ_{SEA} (black), centered on the 12.4-yr period. (d) Wavelet coherence between τ_{AS} and ζ_{SEA} and phase (orange dotted line, in years, where positive values indicate ζ_{SEA} leads) centered on the 12.4-yr period. Phase is only shown where coherence is significant at $p < 0.05$. (e) As Fig. 9d, for ζ_{SEA} and τ_{CP} (blue box in Fig. 8a). The ζ_{SEA} is detrended relative sea level at the Seattle, Washington (U.S.), tide gauge.

over the tip of Greenland, which would drive southerly Labrador Sea wind anomalies, anomalously warm air temperatures, and reductions in Q_{LS}, show a similar leading relationship. Similarly, positive SST anomalies in the central tropical Pacific

are associated with positive τ_{CP} and negative P_S anomalies to their east, and positive ζ along the western North American coast with only a slight lag. These relationships are consistent with the tight coupling evident over shorter (i.e., ENSO) time scales in the Pacific.

4. Discussion

a. Limitations of the tide gauge record

Here, I have shown that decadal ζ variability is amplified, and coherent, in geographically distant coastal locations in the second half of the twentieth century. While tide gauge records provide a unique and stable observational record of this shift, its global spatial structure remains obscured by the sparsity of long tide gauge records outside of North America and Europe (Fig. 1d). However, evidence for globally coherent surface pressure and wind patterns (Figs. 4 and 10) suggests that these results may comprise a lower bound on the spatial coherence of ζ variability along global coastlines during this epoch. Global numerical models (with an adequate representation of climate and coastal sea level variability, where records exist) might be employed to assess the full spatial expression in, for example, the Southern Hemisphere.

While the principal focus of this analysis concerns geographic regions that experience enhanced ζ power and coherence in the late twentieth century, it is important to note that regions exhibiting low ζ power in this epoch may also be influenced by globally coherent climate variability, either due to 1) decreased power in forcing fields or 2) the compensating effects of different forcings. For example, the leading relationship of $\nabla \times \tau$ in the central North Atlantic subtropical gyre (orange box in Fig. 7b) would be expected to drive a decrease in ζ along the southeastern United States coastline approximately contemporaneously with (opposite signed) coastally propagating signals associated with ζ_{NE} (Calafat et al. 2018; Hong et al. 2000). Such offsetting drivers provide a possible explanation for the diverging trends in decadal power across Cape Hatteras, evident in Fig. 1 and noted in Little et al. (2021).

Despite the limitations of the tide gauge dataset, these results document relationships between climate and sea level variability that have several important implications, which are described in the remaining sections.

b. Interpretation and prediction of climate variability

This analysis indicates that the spatial pattern and amplitude of decadal climate variability are strongly time-varying: Broadly, the late twentieth century was characterized by coherent variability across all ocean basins, while limited interbasin connectivity is evident before ~1950. While this finding is contingent upon the quality of the 20CR3, the ERA-20C reanalysis (Poli et al. 2016; not shown) provides similar results. Agreement between these products does not eliminate the possibility of systematic bias in the early twentieth century, however, which underscores the importance of evidence for enhanced decadal variability and coherence in tide gauge records.
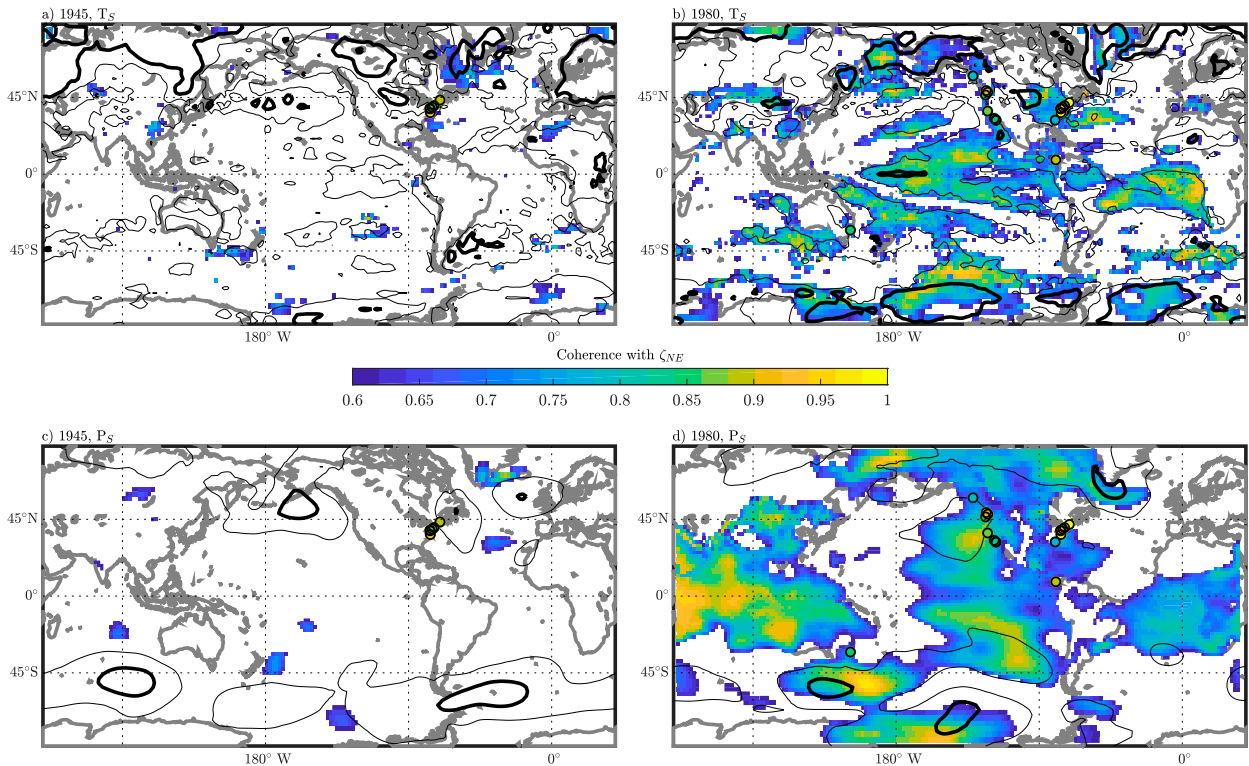
FIG. 10. (a) Wavelet coherence (shading) between ζ_{NE} and surface temperature (T_S) from 20CR3, on a 2° horizontal grid, centered on a period of 12.4 years and the year 1945. (b) As in (a), but centered on the year 1980. Contours in (a) and (b) are wavelet power in T_S; the thick (thin) line is 1 K^2 (0.2 K^2). (c),(d) As in (a) and (b), but for wavelet coherence between ζ_{NE} and P_S. Contours in (c) and (d) are the wavelet power in P_S; the thick (thin) line is 10 $mbar^2$ (2 $mbar^2$).

As noted in the introduction, other studies have found evidence for enhanced decadal variability in the second half of the twentieth century, largely by analyzing central Pacific SSTs. The similar temporal evolution of power in CP SSTs and ζ, and their coherence (Fig. 10), confirm the value of ζ as a complementary indicator. Furthermore, the global extent of coherent changes in SSTs and the near-surface atmospheric state (Figs. 4 and 10) is consistent with evidence for other, remote, aspects of climate that show enhanced variability (e.g., hydroclimate). It also implies that other quantities, yet to be documented, may also be influenced by this nonstationarity.

After ~1990, decadal power in some ζ and surface climate records (and/or their coherence) decreases. However, power continues to increase through the period of record in other records (e.g., τ_{CP}). It thus remains unclear whether nonstationarity is driven by multidecadal to centennial modulation (e.g., associated with Atlantic multidecadal variability; Zhang et al. 2019) or a longer-term, secular, change. Although limited in their ability to capture multiple "cycles" of decadal variability, more detailed analyses over the satellite altimetry era (after 1993) may identify whether more recent climate variability, and/or ζ forcings, are consistent with those identified here between 1950 and 1990.

Regardless, these results imply that different physical processes, interactions, and/or geographic regions exert control on aspects of decadal variability through the historical record.

This, in turn, implies that predictability, apparent predictive skill, and the societal value of predictions, will vary depending upon the time period considered (or utilized for skill assessment). These implications apply broadly to many societally relevant climate variables, and more specifically, to coastal sea level.

For example, conclusions about the drivers and spatial structure of decadal ζ variability in the late twentieth century used in reconstructions (Dangendorf et al. 2021; Piecuch et al. 2018b) and/or "indices" of climate and ocean variability (Ezer 2015; McCarthy et al. 2015) may not apply to other epochs. Looking forward, the relatively large amplitude and spatial scale of decadal ζ variability exhibited in the late twentieth century comprises a promising target for improving predictions of coastal flooding—if such potential predictability is relevant outside this epoch.

c. Mechanisms driving decadal climate variability and its nonstationarity

While I leave the identification of causal mechanisms underlying the periodicity of decadal climate variability and the emergence of global coherence for further work, collectively, these results point to a key role for the tropical oceans. Supporting evidence includes 1) strong coherence between winds and SSTs in both the tropical Pacific and Atlantic Oceans (Figs. 4b and 10b) and 2) poleward-reaching P_S anomalies
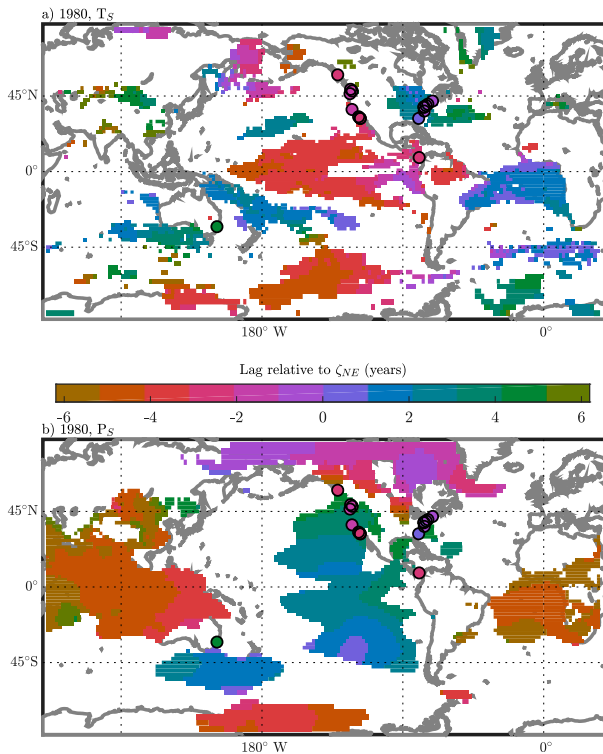
a) 1980, T_S

Lag relative to ζ_{NE} (years)

b) 1980, P_S

FIG. 11. (a) The phase lag between ζ_{NE} and T_S (yr, where positive values indicate ζ_{NE} leads). (b) As in (a), but for the phase lag between ζ_{NE} and P_S. Phase is only shown where coherence (Fig. 10) is greater than 0.7.

indicative of stationary atmospheric Rossby wave responses to tropical variability (Fig. 11b).

Increases in CP SST variability have been highlighted as an important driver of extratropical variability in the late twentieth century, although it is unclear whether extratropical changes are driven by increases in SST power (Chunhan et al. 2021; Sun and Yu 2009) or changes in the dynamics of extratropical teleconnections (e.g., Fuentes-Franco et al. 2022; Graf and Zanchettin 2012; Soulard et al. 2019). I have shown evidence from 20CR3, consistent with previous analyses, indicating a dramatic increase in power in CP SSTs. However, the teleconnections in Fig. 11b are more consistent with an origin in the Indian Ocean. Given the extensive interbasin coherence, and the tight coupling between the tropical atmosphere and ocean, it seems plausible that increases in CP SST variability are response to increases in decadal variability initiated and/or modulated in other tropical oceans.

Although I have not explicitly related spatiotemporal patterns of variability shown here to known climate modes, it is worth noting the absence of coherence between ζ_{NE} and NAO indices at approximately decadal frequency bands (Fig. 12). The NAO has been linked to ζ_{NE}, as well as its local and remote atmospheric forcing mechanisms, over interannual time scales. Evidence for epochs of coherence between ζ_{NE} and a station-based wintertime NAO index (Fig. 12c) at interannual time scales are supportive of prior work. However, at
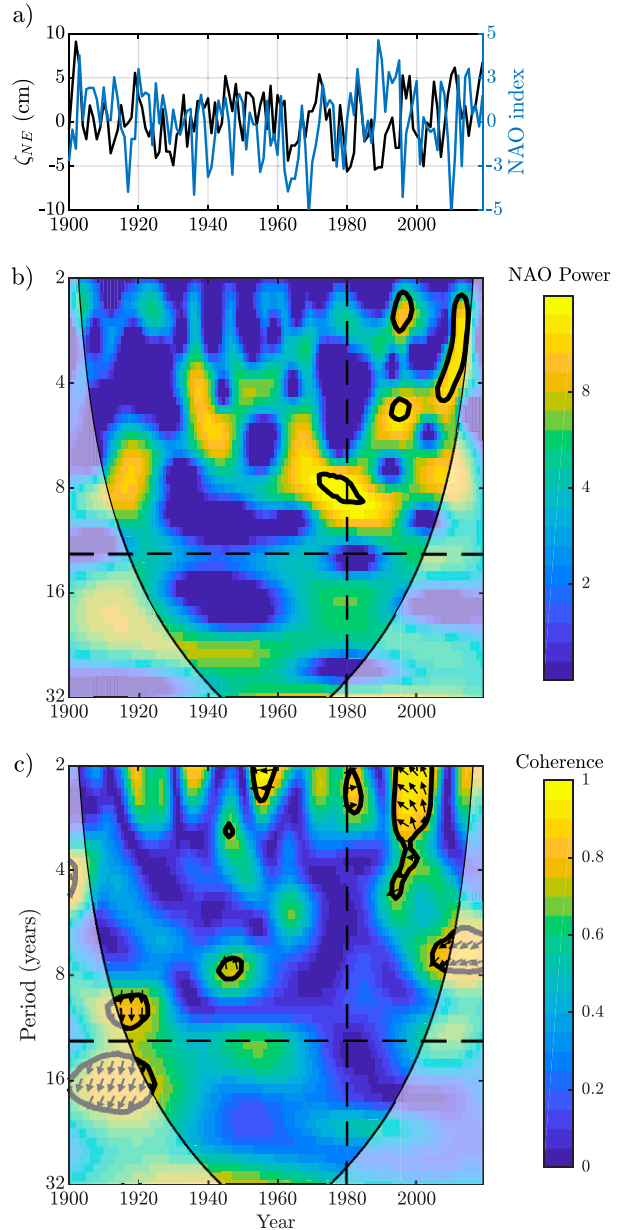

FIG. 12. (a) The ζ_{NE} (black) and a station-based wintertime (December–March) NAO index, 1900–2019. (b) Wavelet power; as in Fig. 1b, but for the NAO index. (c) Wavelet coherence; as in Fig. 2b, but between ζ_{NE} and the NAO index.

decadal frequencies, ζ_{NE} does not exhibit significant coherence with NAO, nor does NAO exhibit significantly enhanced power (results are insensitive to season and/or formulations of the NAO index).

One plausible explanation for the lack of a relationship is that the processes controlling variability at decadal frequencies are independent of NAO. Another is that the variability described here is related to a shift in the position of NAO centers of action, occurring at lower frequencies than those that dominate the power in NAO indices. Indeed, nonstationary

relationships between ζ_{NE} and NAO have been documented in previous studies (Andres et al. 2013) and attributed to shifts with respect to orientation of alongshore winds (Kenigson et al. 2018). These results indicate that such a shift might also influence the role of different drivers of ζ_{NE}, by initiating strong buoyancy-driven variability originating in the Labrador Sea.

d. Mechanisms linking coastal sea level to surface forcing

I have focused analysis on ζ variability and its drivers along the eastern and western North American coastlines, where a long and spatially resolved tide gauge record is available. If global models are available that adequately represent both climate and coastal sea level variability, they will be valuable for more definitively identifying the mechanisms relating global climate to observed decadal sea level variability, in these and other regions.

However, partial insights can be gleaned from regional models and/or perturbation studies. The decadal coherence between ζ_{NE} and Q_{LS} is a prime target for such studies. In contrast to the relatively simple dynamics linking equatorial and alongshore wind stress to ζ along the western North American coastline, there are multiple plausible causal mechanisms underlying coherence with Q_{LS}. These include 1) Rossby wave- and/or advection-mediated communication of offshore sea level signals to the Labrador coastline, with subsequent equatorward propagation (e.g., Minobe et al. 2017; Roussenov et al. 2008; Wang et al. 2022); 2) interaction of offshore shelf/slope and deep western boundary currents with the Gulf Stream, recirculation gyres, and/or eddies, between the tail of the Grand Banks and Cape Hatteras (e.g., Gonçalves Neto et al. 2021; Peterson et al. 2017; Saba et al. 2016; Zhang and Vallis 2007); and 3) changes in upstream shelf currents and/or continental shelf hydrography (either due to atmospheric forcings that are correlated across shelf and offshore regions, or advection of offshore water masses onto the shelf) (New et al. 2021; Xu and Oey 2011; Yang and Chen 2021).

Within the precision of this analysis, each of these pathways is consistent with the lag between ζ_{NE} and Q_{LS} (Fig. 6). Modeling studies are required to investigate the governing dynamics, including whether the amplitude of sea level anomalies associated with each mechanism is sufficient to account for observed ζ_{NE} anomalies. They may also be used to assess any role for upstream preconditioning of Labrador Sea water masses, assuming dense water formation is a critical element in ζ_{NE} variability. Although the motivation for, and validation of, such studies may originate in the observed decadal variability, key processes are likely to remain relevant over longer time scales.

5. Conclusions

This study identifies a dramatic increase in the amplitude and spatial coherence of decadal (11–14-yr period) sea level variability between approximately 1960 and 2000. In this frequency band and epoch, western North American sea level is approximately out of phase with sea level at Sydney, Australia, and leads northeast United States sea level by 1–2 years. Coastal sea level variability is related to globally coherent changes in surface forcing fields; its amplitude and phase are determined by the nature of regional forcing (e.g., local or remote, wind stress or heat flux) and the favored propagation pathways of sea level anomalies. Remote equatorial and local alongshore wind stress forcings are most consistent with observed decadal variability along the western North American coastline, while Labrador Sea heat fluxes are most consistent with the late twentieth-century enhancement of decadal coastal sea level variability in the northeast United States.

Enhanced coastal sea level variability is associated with increased global coherence of, and order-of-magnitude increases in, tropical SST variability and teleconnected extratropical pressure fields. These results thus extend the spatial scale and set of variables showing a systematic increase in the amplitude of decadal climate variability over the twentieth century, and point to a tropical origin. The broad implications of this nonstationarity for decadal predictability and interpretation of the historical record underscore the need to understand mechanisms regulating its periodic behavior, increasing amplitude, and response to changes in background climate state, such as that expected in the twenty-first century. Where tide gauges exist, the long coastal sea level record may offer further insights into underlying drivers and impacts, however, it will remain spatially sparse. More definitive understanding will require long, coupled, numerical simulations, for which coastal sea level records may act as a key constraint.

Data availability statement. Tide gauge data are freely available from the Permanent Service for Mean Sea Level (http://www.psmsl.org/data/obtaining/). Output from the Twentieth Century Reanalysis Project version 3 is freely available from NOAA's Physical Sciences Laboratory (https://psl.noaa.gov/data/20thC_Rean/). North Atlantic Oscillation indices are available through the National Center for Atmospheric Research's Climate Data Guide (https://climatedataguide.ucar.edu/climate-data/).

REFERENCES

Andres, M., G. G. Gawarkiewicz, and J. M. Toole, 2013: Interannual sea level variability in the western North Atlantic: Regional forcing and remote response. *Geophys. Res. Lett.*, **40**, 5915–5919, https://doi.org/10.1002/2013GL058013.

Branstator, G., 2002: Circumglobal teleconnections, the jet stream waveguide, and the North Atlantic oscillation. *J. Climate*, **15**,

1893–1910, https://doi.org/10.1175/1520-0442(2002)015<1893:CTTJSW>2.0.CO;2.

Brassington, G. B., 1997: The modal evolution of the southern oscillation. *J. Climate*, **10**, 1021–1034, https://doi.org/10.1175/1520-0442(1997)010<1021:TMEOTS>2.0.CO;2.

Cai, W., and Coauthors, 2019: Pantropical climate interactions. *Science*, **363**, eaav4236, https://doi.org/10.1126/science.aav4236.

Calafat, F. M., T. Wahl, F. Lindsten, J. Williams, and E. Frajka-Williams, 2018: Coherent modulation of the sea-level annual cycle in the United States by Atlantic Rossby waves. *Nat. Commun.*, **9**, 2571, https://doi.org/10.1038/s41467-018-04898-y.

Chafik, L., J. E. O. Nilsen, S. Dangendorf, G. Reverdin, and T. Frederikse, 2019: North Atlantic Ocean circulation and decadal sea level change during the altimetry era. *Sci. Rep.*, **9**, 1041, https://doi.org/10.1038/s41598-018-37603-6.

Chelton, D. B., and R. E. Davis, 1982: Monthly mean sea-level variability along the west coast of North America. *J. Phys. Oceanogr.*, **12**, 757–784, https://doi.org/10.1175/1520-0485(1982)012<0757:MMSLVA>2.0.CO;2.

Chunhan, J., W. Bin, and L. Jian, 2021: Emerging Pacific quasi-decadal oscillation over the past 70 years. *Geophys. Res. Lett.*, **48**, e2020GL090851, https://doi.org/10.1029/2020GL090851.

Dangendorf, S., M. Marcos, G. Wöppelmann, C. P. Conrad, T. Frederikse, and R. Riva, 2017: Reassessment of 20th century global mean sea level rise. *Proc. Natl. Acad. Sci. USA*, **114**, 5946–5951, https://doi.org/10.1073/pnas.1616007114.

——, T. Frederikse, L. Chafik, J. M. Klinck, T. Ezer, and B. D. Hamlington, 2021: Data-driven reconstruction reveals large-scale ocean circulation control on coastal sea level. *Nat. Climate Change*, **11**, 514–520, https://doi.org/10.1038/s41558-021-01046-1.

Enfield, D. B., and J. S. Allen, 1980: On the structure and dynamics of monthly mean sea level anomalies along the Pacific coast of North and South America. *J. Phys. Oceanogr.*, **10**, 557–578, https://doi.org/10.1175/1520-0485(1980)010<0557:OTSADO>2.0.CO;2.

Ezer, T., 2015: Detecting changes in the transport of the Gulf Stream and the Atlantic overturning circulation from coastal sea level data: The extreme decline in 2009–2010 and estimated variations for 1935–2012. *Global Planet. Change*, **129**, 23–36, https://doi.org/10.1016/j.gloplacha.2015.03.002.

Frederikse, T., K. Simon, C. A. Katsman, and R. Riva, 2017: The sea-level budget along the northwest Atlantic coast: GIA, mass changes, and large-scale ocean dynamics. *J. Geophys. Res. Oceans*, **122**, 5486–5501, https://doi.org/10.1002/2017JC012699.

Fuentes-Franco, R., T. Koenigk, D. Docquier, F. Graef, and K. Wyser, 2022: Exploring the influence of the North Pacific Ocean Rossby wave sources on interannual variability of summer precipitation and surface temperature over the Northern Hemisphere. *Climate Dyn.*, **59**, 2025–2039, https://doi.org/10.1007/s00382-022-06194-4.

Gonçalves Neto, A., J. A. Langan, and J. B. Palter, 2021: Changes in the Gulf Stream preceded rapid warming of the northwest Atlantic shelf. *Commun. Earth Environ.*, **2**, 74, https://doi.org/10.1038/s43247-021-00143-5.

Graf, H.-F., and D. Zanchettin, 2012: Central Pacific El Niño, the "subtropical bridge," and Eurasian climate. *J. Geophys. Res.*, **117**, D01102, https://doi.org/10.1029/2011JD016493.

Grinsted, A., J. C. Moore, and S. Jevrejeva, 2004: Application of the cross wavelet transform and wavelet coherence to geophysical time series. *Nonlinear Processes Geophys.*, **11**, 561–566, https://doi.org/10.5194/npg-11-561-2004.

Han, W., and Coauthors, 2014: Intensification of decadal and multi-decadal sea level variability in the western tropical Pacific during recent decades. *Climate Dyn.*, **43**, 1357–1379, https://doi.org/10.1007/s00382-013-1951-1.

——, and Coauthors, 2019: Impacts of basin-scale climate modes on coastal sea level: A review. *Surv. Geophys.*, **40**, 1493–1541, https://doi.org/10.1007/s10712-019-09562-8.

Henley, B. J., J. Gergis, D. J. Karoly, S. Power, J. Kennedy, and C. K. Folland, 2015: A tripole index for the interdecadal Pacific oscillation. *Climate Dyn.*, **45**, 3077–3090, https://doi.org/10.1007/s00382-015-2525-1.

Higuchi, K., J. Huang, and A. Shabbar, 1999: A wavelet characterization of the North Atlantic oscillation variation and its relationship to the North Atlantic sea surface temperature. *Int. J. Climatol.*, **19**, 1119–1129, https://doi.org/10.1002/(SICI)1097-0088(199908)19:10<1119::AID-JOC414>3.0.CO;2-7.

Holgate, S. J., and Coauthors, 2013: New data systems and products at the permanent service for mean sea level. *J. Coastal Res.*, **29**, 493–504, https://doi.org/10.2112/JCOASTRES-D-12-00175.1.

Hong, B. G., W. Sturges, and A. J. Clarke, 2000: Sea level on the U.S. East Coast: Decadal variability caused by open ocean wind-curl forcing. *J. Phys. Oceanogr.*, **30**, 2088–2098, https://doi.org/10.1175/1520-0485(2000)030<2088:SLOTUS>2.0.CO;2.

Kao, H.-Y., and J.-Y. Yu, 2009: Contrasting eastern-Pacific and central-Pacific types of ENSO. *J. Climate*, **22**, 615–632, https://doi.org/10.1175/2008JCLI2309.1.

Kenigson, J. S., W. Han, B. Rajagopalan, Yanto, and M. Jasinski, 2018: Decadal shift of NAO-linked interannual sea level variability along the U.S. northeast coast. *J. Climate*, **31**, 4981–4989, https://doi.org/10.1175/JCLI-D-17-0403.1.

Kopp, R. E., and Coauthors, 2016: Temperature-driven global sea-level variability in the common era. *Proc. Natl. Acad. Sci. USA*, **113**, E1434–E1441, https://doi.org/10.1073/pnas.1517056113.

Le Bras, I. A., I. Yashayaev, and J. M. Toole, 2017: Tracking Labrador Sea water property signals along the deep western boundary current. *J. Geophys. Res. Oceans*, **122**, 5348–5366, https://doi.org/10.1002/2017JC012921.

Lee, J.-Y., and Coauthors, 2021: Future global climate: Scenario-based projections and near-term information. *Climate Change 2021: The Physical Science Basis*, K. K. Kanikicharla, V. Kattsov, and M. Kimoto, Eds., Cambridge University Press, 553–672.

Lee, T., and M. J. McPhaden, 2010: Increasing intensity of El Niño in the central-equatorial Pacific. *Geophys. Res. Lett.*, **37**, L14603, https://doi.org/10.1029/2010GL044007.

Li, X., and Coauthors, 2021: Tropical teleconnection impacts on Antarctic climate changes. *Nat. Rev. Earth Environ.*, **2**, 680–698, https://doi.org/10.1038/s43017-021-00204-5.

Li, Y., R. Ji, P. S. Fratantoni, C. Chen, J. A. Hare, C. S. Davis, and R. C. Beardsley, 2014: Wind-induced interannual variability of sea level slope, along-shelf flow, and surface salinity on the Northwest Atlantic shelf. *J. Geophys. Res. Oceans*, **119**, 2462–2479, https://doi.org/10.1002/2013JC009385.

Little, C. M., C. G. Piecuch, and R. M. Ponte, 2017: On the relationship between the meridional overturning circulation, alongshore wind stress, and United States East Coast sea level in the Community Earth System Model large ensemble. *J. Geophys. Res. Oceans*, **122**, 4554–4568, https://doi.org/10.1002/2017JC012713.

——, A. Hu, C. W. Hughes, G. D. McCarthy, C. G. Piecuch, R. M. Ponte, and M. D. Thomas, 2019: The relationship between U.S. East Coast sea level and the Atlantic meridional overturning circulation: A review. *J. Geophys. Res. Oceans*, **124**, 6435–6458, https://doi.org/10.1029/2019JC015152.

——, C. G. Piecuch, and R. M. Ponte, 2021: North American East Coast sea level exhibits high power and spatiotemporal complexity on decadal timescales. *Geophys. Res. Lett.*, **48**, e2021GL093675, https://doi.org/10.1029/2021GL093675.

Liu, C., W. Zhang, M. F. Stuecker, and F. F. Jin, 2019: Pacific meridional mode–western North Pacific tropical cyclone linkage explained by tropical Pacific quasi-decadal variability. *Geophys. Res. Lett.*, **46**, 13 346–13 354, https://doi.org/10.1029/2019GL085340.

Liu, Y., and Coauthors, 2017: Recent enhancement of central Pacific El Niño variability relative to last eight centuries. *Nat. Commun.*, **8**, 15386, https://doi.org/10.1038/ncomms15386.

Lyu, K., X. Zhang, J. A. Church, J. Hu, and J.-Y. Yu, 2017: Distinguishing the quasi-decadal and multidecadal sea level and climate variations in the Pacific: Implications for the ENSO-like low-frequency variability. *J. Climate*, **30**, 5097–5117, https://doi.org/10.1175/JCLI-D-17-0004.1.

Martín-Rey, M., B. Rodríguez-Fonseca, I. Polo, and F. Kucharski, 2014: On the Atlantic–Pacific Niños connection: A multidecadal modulated mode. *Climate Dyn.*, **43**, 3163–3178, https://doi.org/10.1007/s00382-014-2305-3.

——, I. Polo, B. Rodríguez-Fonseca, T. Losada, and A. Lazar, 2018: Is there evidence of changes in tropical Atlantic variability modes under AMO phases in the observational record? *J. Climate*, **31**, 515–536, https://doi.org/10.1175/JCLI-D-16-0459.1.

McCarthy, G. D., I. D. Haigh, J. J.-M. Hirschi, J. P. Grist, and D. A. Smeed, 2015: Ocean impact on decadal Atlantic climate variability revealed by sea-level observations. *Nature*, **521**, 508–510, https://doi.org/10.1038/nature14491.

Meehl, G. A., and Coauthors, 2021: Atlantic and Pacific tropics connected by mutually interactive decadal-timescale processes. *Nat. Geosci.*, **14**, 36–42, https://doi.org/10.1038/s41561-020-00669-x.

Minobe, S., M. Terada, B. Qiu, and N. Schneider, 2017: Western boundary sea level: A theory, rule of thumb, and application to climate models. *J. Phys. Oceanogr.*, **47**, 957–977, https://doi.org/10.1175/JPO-D-16-0144.1.

New, A. L., D. A. Smeed, A. Czaja, A. T. Blaker, J. V. Mecking, J. P. Mathews, and A. Sanchez-Franks, 2021: Labrador slope water connects the subarctic with the Gulf Stream. *Environ. Res. Lett.*, **16**, 084019, https://doi.org/10.1088/1748-9326/ac1293.

Nigam, S., A. Sengupta, and A. Ruiz-Barradas, 2020: Atlantic–Pacific links in observed multi-decadal SST variability: Is the Atlantic multidecadal oscillation's phase reversal orchestrated by the Pacific decadal oscillation? *J. Climate*, **33**, 5479–5505, https://doi.org/10.1175/JCLI-D-19-0880.1.

Peterson, I., B. Greenan, D. Gilbert, and D. Hebert, 2017: Variability and wind forcing of ocean temperature and thermal fronts in the slope water region of the northwest Atlantic. *J. Geophys. Res. Oceans*, **122**, 7325–7343, https://doi.org/10.1002/2017JC012788.

Piecuch, C. G., S. Dangendorf, R. M. Ponte, and M. Marcos, 2016: Annual sea level changes on the North American northeast coast: Influence of local winds and barotropic motions. *J. Climate*, **29**, 4801–4816, https://doi.org/10.1175/JCLI-D-16-0048.1.

——, K. Bittermann, A. C. Kemp, R. M. Ponte, C. M. Little, S. E. Engelhart, and S. J. Lentz, 2018a: River-discharge effects on United States Atlantic and Gulf coast sea-level changes. *Proc. Natl. Acad. Sci. USA*, **115**, 7729–7734, https://doi.org/10.1073/pnas.1805428115.

——, P. Huybers, C. C. Hay, A. C. Kemp, C. M. Little, J. X. Mitrovica, R. M. Ponte, and M. P. Tingley, 2018b: Origin of spatial variation in US East Coast sea-level trends during 1900–2017. *Nature*, **564**, 400–404, https://doi.org/10.1038/s41586-018-0787-6.

Poli, P., and Coauthors, 2016: ERA-20C: An atmospheric reanalysis of the twentieth century. *J. Climate*, **29**, 4083–4097, https://doi.org/10.1175/JCLI-D-15-0556.1.

Power, S., and Coauthors, 2021: Decadal climate variability in the tropical Pacific: Characteristics, causes, predictability, and prospects. *Science*, **374**, eaay9165, https://doi.org/10.1126/science.aay9165.

Roussenov, V. M., R. G. Williams, C. W. Hughes, and R. J. Bingham, 2008: Boundary wave communication of bottom pressure and overturning changes for the North Atlantic. *J. Geophys. Res.*, **113**, C08042, https://doi.org/10.1029/2007JC004501.

Saba, V. S., and Coauthors, 2016: Enhanced warming of the northwest Atlantic Ocean under climate change. *J. Geophys. Res. Oceans*, **121**, 118–132, https://doi.org/10.1002/2015JC011346.

Seneviratne, S. I., and Coauthors, 2012: Changes in climate extremes and their impacts on the natural physical environment. *Managing the Risks of Extreme Events and Disasters to Advance Climate Change Adaptation*, C. B. Field et al., Eds., Cambridge University Press, 109–230.

——, and Coauthors, 2021: Weather and climate extreme events in a changing climate. *Climate Change 2021: The Physical Science Basis*, V. Masson-Delmotte et al., Eds., Cambridge University Press, 1531–1766, https://doi.org/10.1017/9781009157896.013.

Slivinski, L. C., and Coauthors, 2019: Towards a more reliable historical reanalysis: Improvements for version 3 of the Twentieth Century Reanalysis system. *Quart. J. Roy. Meteor. Soc.*, **145**, 2876–2908, https://doi.org/10.1002/qj.3598.

Soulard, N., H. Lin, and B. Yu, 2019: The changing relationship between ENSO and its extratropical response patterns. *Sci. Rep.*, **9**, 6507, https://doi.org/10.1038/s41598-019-42922-3.

Stammer, D., A. Cazenave, R. M. Ponte, and M. E. Tamisiea, 2013: Causes for contemporary regional sea level changes. *Annu. Rev. Mar. Sci.*, **5**, 21–46, https://doi.org/10.1146/annurev-marine-121211-172406.

Sullivan, A., J.-J. Luo, A. C. Hirst, D. Bi, W. Cai, and J. He, 2016: Robust contribution of decadal anomalies to the frequency of central-Pacific El Niño. *Sci. Rep.*, **6**, 38540, https://doi.org/10.1038/srep38540.

Sun, F., and J.-Y. Yu, 2009: A 10–15-yr modulation cycle of ENSO intensity. *J. Climate*, **22**, 1718–1735, https://doi.org/10.1175/2008JCLI2285.1.

Thompson, K. R., 1986: North Atlantic sea-level and circulation. *Geophys. J. Int.*, **87**, 15–32, https://doi.org/10.1111/j.1365-246X.1986.tb04543.x.

Thompson, P. R., M. A. Merrifield, J. R. Wells, and C. M. Chang, 2014: Wind-driven coastal sea level variability in the northeast Pacific. *J. Climate*, **27**, 4733–4751, https://doi.org/10.1175/JCLI-D-13-00225.1.

Wang, O., and Coauthors, 2022: Local and remote forcing of interannual sea-level variability at Nantucket island. *J. Geophys. Res. Oceans*, **127**, e2021JC018275, https://doi.org/10.1029/2021JC018275.

Wang, S.-Y., R. R. Gillies, J. Jin, and L. E. Hipps, 2010: Coherence between the Great Salt Lake level and the Pacific quasi-decadal oscillation. *J. Climate*, **23**, 2161–2177, https://doi.org/10.1175/2009JCLI2979.1.

——, K. Hakala, R. R. Gillies, and W. J. Capehart, 2014: The Pacific quasi-decadal oscillation (QDO): An important precursor toward anticipating major flood events in the Missouri

River Basin? *Geophys. Res. Lett.*, **41**, 991–997, https://doi.org/10.1002/2013GL059042.

Woodworth, P. L., M. A. Morales Maqueda, W. R. Gehrels, V. M. Roussenov, R. G. Williams, and C. W. Hughes, 2017: Variations in the difference between mean sea level measured either side of Cape Hatteras and their relation to the North Atlantic oscillation. *Climate Dyn.*, **49**, 2451–2469, https://doi.org/10.1007/s00382-016-3464-1.

——, and Coauthors, 2019: Forcing factors affecting sea level changes at the coast. *Surv. Geophys.*, **40**, 1351–1397, https://doi.org/10.1007/s10712-019-09531-1.

Xu, F.-H., and L.-Y. Oey, 2011: The origin of along-shelf pressure gradient in the middle Atlantic bight. *J. Phys. Oceanogr.*, **41**, 1720–1740, https://doi.org/10.1175/2011JPO4589.1.

Yang, J., and K. Chen, 2021: The role of wind stress in driving the along-shelf flow in the northwest Atlantic Ocean. *J. Geophys. Res. Oceans*, **126**, e2020JC016757, https://doi.org/10.1029/2020JC016757.

Zhang, R., and G. K. Vallis, 2007: The role of bottom vortex stretching on the path of the North Atlantic western boundary current and on the northern recirculation gyre. *J. Phys. Oceanogr.*, **37**, 2053–2080, https://doi.org/10.1175/JPO3102.1.

——, R. Sutton, G. Danabasoglu, Y. O. Kwon, R. Marsh, S. G. Yeager, D. E. Amrhein, and C. M. Little, 2019: A review of the role of the Atlantic meridional overturning circulation in Atlantic multidecadal variability and associated climate impacts. *Rev. Geophys.*, **57**, 316–375, https://doi.org/10.1029/2019RG000644.